Article

Combined First-Principles and Experimental Investigation into the Reactivity of Codeposited Chromium−Carbon under Pressure

Paul V. Marshall,[||] Scott D. Thiel,[||] Elizabeth E. Cote, Rostislav Hrubiak, Matthew L. Whitaker, Yue Meng, and James P. S. Walsh*

Cite This: https://doi.org/10.1021/acsmaterialsau.3c00086

Read Online

| ACCESS | | Metrics & More | | Article Recommendations | | SI Supporting Information |

ABSTRACT: High-pressure synthesis in the diamond anvil cell suffers from the lack of a general approach for the control of precursor stoichiometry and homogeneity. Here, we present results from a new method we have developed that uses magnetron cosputtering to prepare stoichiometrically precise and atomically mixed amorphous films of Cr:C. Laser-heated diamond anvil cell experiments carried out on a flake of this sample at pressures between 13.5 and 24.3 GPa lead to the observation of Cr_3C (*Pnma*) over the entire pressure range—in good agreement with our in-house theoretical predictions—but also reveal two other metastable phases that were not expected: a novel monoclinic chromium carbide phase and the NaCl-type CrC ($Fm\bar{3}m$) phase. The unexpected stability of CrC is investigated by using first-principles methods, revealing a large stabilizing effect tied to substoichiometry at the carbon site. These results offer an important case study into the current limitations of crystal structure prediction methods with regard to phase complexity and bolster the growing need for advanced theoretical approaches that can more completely survey experimentally unexplored phase space.

KEYWORDS: high pressure, diamond anvil cell, solid-state synthesis, density functional theory, transition metal carbides
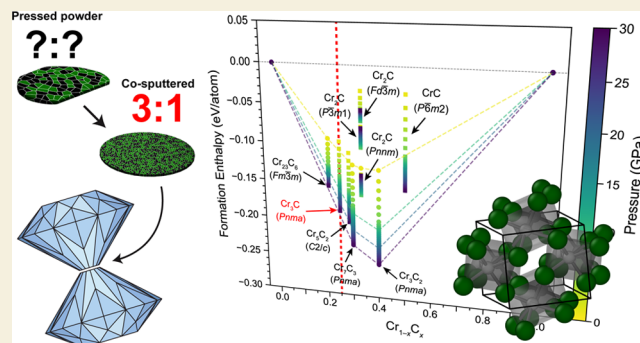
INTRODUCTION

Transition metal carbides (TMCs) find widespread use throughout industry due to their impressive high-resilience properties, which often include a combination of high melting points, microhardness, high thermal and electrical conductivity, and corrosion resistance.[1−5] These properties are especially pronounced in chromium carbides, which are used in a broad range of demanding applications. For example, Cr_3C_2 (*Pnma*) embedded within a NiCr binder is used for high-temperature and oxidation-resistant coatings in steam and gas turbines;[6,7] Cr_7C_3 (*Pnma*) excels as a wear- and heat-resistant coating in bearing shafts, seals, and furnaces;[8−11] self-lubricating nanocomposites of amorphous CrC_y and the nanocrystalline NaCl-type $CrC_{(1−x)}$ ($Fm\bar{3}m$) thin films are promising materials for replacing noble metals in sliding electrical contacts;[12] and Cr_3C_2 (*Pnma*) embedded within carbon nanofibers shows improved cycling stability compared with conventional lithium/sulfur batteries.[13]

The chromium−carbon binary system contains three thermodynamically stable compounds (Figure 1): Cr_3C_2 (*Pnma*),[14,15] $Cr_{23}C_6$ ($Fm\bar{3}m$),[16,17] and Cr_7C_3 (*Pnma*).[18,19] It also contains a number of metastable phases that cannot be accessed with traditional solid-state methods, including cementite Cr_3C (*Pnma*), which has been observed in small quantities following splat quenching;[20,21] Cr_2C ($P6_3/mmc$),

which has been detected within iron alloys enriched with chromium;[22,23] the Hägg carbide isomorph, Cr_5C_2 (*C2/c*), which has been prepared by reactive sputtering;[24,25] the "filled Re$_3$B-type" Cr_3C_2 (*Cmcm*), which has also been observed with reactive sputtering;[26,27] and finally the NaCl-type $CrC_{(1−x)}$ ($Fm\bar{3}m$), which has been detected in reactive sputtering, ion-implantation experiments, and salt flux reactions.[28−30] The large number of phases within the binary Cr−C system is remarkable and provides a solid foundation for chemists to study how the impressive high-resilience bulk properties are tied to crystal structures within this class of materials. Although many of the metastable chromium carbide phases have been structurally characterized, the recovery of samples suitable for bulk property characterization has remained a significant challenge.

To address this challenge, we turned to a high-pressure synthesis. This approach has proven to be one of the most productive methods for the bulk synthesis of metastable
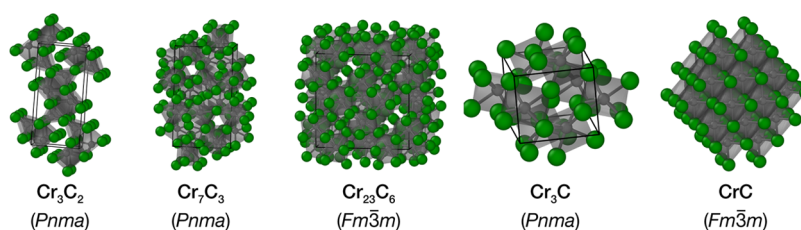
A

Figure 1. Crystal structures of selected chromium carbides. Polyhedra highlight the local coordination geometry around the carbon atoms (dark gray) bonded to chromium atoms (dark green). Cr_3C_2 ($Pnma$), Cr_7C_3 ($Pnma$), and $Cr_{23}C_6$ ($Fm\bar{3}m$) are thermodynamically stable, while Cr_3C ($Pnma$) and CrC ($Fm\bar{3}m$) are both metastable phases.

compounds that cannot be accessed with traditional heating methods, and in fact, it has already had demonstrable success in the discovery of bulk transition metal carbide phases.[31−40]

We report here a study into the high-pressure phase space of the Cr−C binary system between pressures of 0 and 30 GPa. We begin with a survey of stable Cr−C phases using crystal structure prediction methods, which are commonly used to guide experiments by identifying potential synthesis targets. We then introduce a novel precursor sample preparation method that uses magnetron cosputtering of the elements to precisely control composition and mixing within diamond anvil cell experiments. We then return to computational approaches to gain deeper insight and detail on the stability of chromium carbides that we observe in our high-pressure synthesis experiments.

■ METHODS

Computational Details

In order to gauge the stability of a number of potential phases in the chromium carbide system, we performed first-principles density functional theory calculations within CASTEP v22.11.[41] The calculations for the convex hull were performed with CASTEP's default ultrasoft pseudopotential library (C19), a maximum Monkhorst-Pack grid spacing of 0.02 Å^{-1},[42] a plane-wave cutoff energy of 680 eV, and finite basis set corrections. Structures were individually relaxed at each pressure.

Calculations of the phonon modes of Cr_3C ($Pnma$) and CrC ($Fm\bar{3}m$) were performed under the harmonic approximation using the finite displacement method and a supercell, also known as the "direct method."[43−45] These calculations used CASTEP's norm-conserving pseudopotential library (NCP), a maximum Monkhorst-Pack grid spacing of 0.03 Å^{-1}, a cutoff energy of 1600 eV, an acoustic sum rule correction applied in reciprocal space,[46,47] and spin-polarization. Prior to the phonon calculations, the Cr_3C ($Pnma$) structure was relaxed to a force tolerance of 0.0001 eV Å^{-1}. Forces on CrC ($Fm\bar{3}m$) are zero by symmetry.

Additional calculations on the stability of the substoichiometric $CrC_{(1−x)}$ ($Fm\bar{3}m$) system were performed with CASTEP v19.11. These calculations used CASTEP's high-throughput pseudopotential library (QC5), a cutoff energy of 326.5 eV, a maximum Monkhorst-Pack grid spacing of 0.05 Å^{-1}, and finite basis set corrections. We sampled and geometry optimized around 400 vacancy configurations of a 32-Cr atom $2 \times 2 \times 2$ conventional supercell at each pressure of 0 and 20 GPa.

The Perdew−Burke−Ernzerhof (PBE) approach to the generalized gradient approximation of the exchange-correlation functional was used for all density functional theory calculations.[48] The c2x program,[49] atomic simulation environment (ASE) python package,[50] and pymatgen python package[51] were used to convert, manage, and process the inputs and results of calculations. Most initial structures were acquired from the AFLOW Prototype Encyclopedia or web database.[52−55] See the Supporting Information for more in-depth details of the calculations.

Preparation of Cosputtered Precursor Films

Chromium−carbon amorphous films were codeposited by magnetron sputtering (AJA International Orion 8 Sputtering System) onto Si (100) substrates using metallic chromium (99.95%) and carbon graphite (99.999%) targets, both of which were 5.08 cm in diameter and 0.635 cm thick. The chromium and carbon targets were powered by direct current (dc) and radio frequency (RF) magnetron sputtering, respectively. The power of the dc and RF supplies were set at 69 and 240 W, respectively, for the duration of the 10 h deposition. The base pressure of the sputtering chamber was below 3.0×10^{-6} Torr.

Throughout the deposition, the substrate was rotated at 100 rpm and was held 30 cm above the targets in an argon atmosphere with a sputtering pressure of 0.52 Pa. A glovebag filled with N_2 was used to prevent the oxidation of the samples while transferring from the load lock to our argon-filled glovebox. Flakes of these samples were characterized via scanning electron microscopy and energy dispersive spectroscopy using an FEI Magellan 400 XHR-SEM instrument with an Oxford X-MAX 80 mm^2 energy dispersive X-ray spectrometer attachment (Figure S13).

Laser-Heated Diamond Anvil Cell Synthesis

Flakes isolated from the cosputtered samples measuring approximately 90 μm × 90 μm were sandwiched between MgO disks (125 μm in diameter).[31] The MgO disks were loaded into the sample space of rhenium gaskets (originally 250 μm thick) that were preindented to a thickness of 35−45 μm and EDM-drilled to host a 127 μm sample space in the center of the indent. DACs were taken to pressure in our argon-filled glovebox to ensure that the sample space was sealed with an inert environment.

In situ laser heating ($\lambda = 1064$ nm, fwhm ∼ 30 μm) and X-ray diffraction were performed at beamline 16-ID-B at the Advanced Photon Source, Argonne National Laboratory.[56] Samples were heated to 1700−2100 K. The incident X-rays ($\lambda = 0.48593$ Å) were aligned with the heating spot for *in situ* characterization during heating. MgO acted both as a thermal insulator and pressure calibrant.[57] Diffraction patterns were collected every 5 s with a 4.9 s exposure time on a Pilatus 1M-F detector. Temperature was determined by fitting the Planck radiation function to the blackbody radiation (600−800 nm) of the heated sample.[56] The temperature was measured through both sides of the cell, and the average was used for reporting to the nearest 100 K. Dioptas was used for real-time integration of the diffraction patterns.[58] TOPAS-Academic v6 was used to fit the patterns using Rietveld methods (see the Supporting Information for further details). Strongly textured MgO reflections and diamond Bragg reflections were masked before the integrations. Pressures were observed to differ slightly before and after the heating runs, but in all cases, the differences were below ∼1 GPa.

■ RESULTS AND DISCUSSION

Enthalpy Calculations on the Cr−C System

We began our investigation of the Cr−C system by surveying stable phases between 0 and 30 GPa, using an approach that combined (1) a list of known stable phases in the Cr−C system along with simple and common phases in other binary
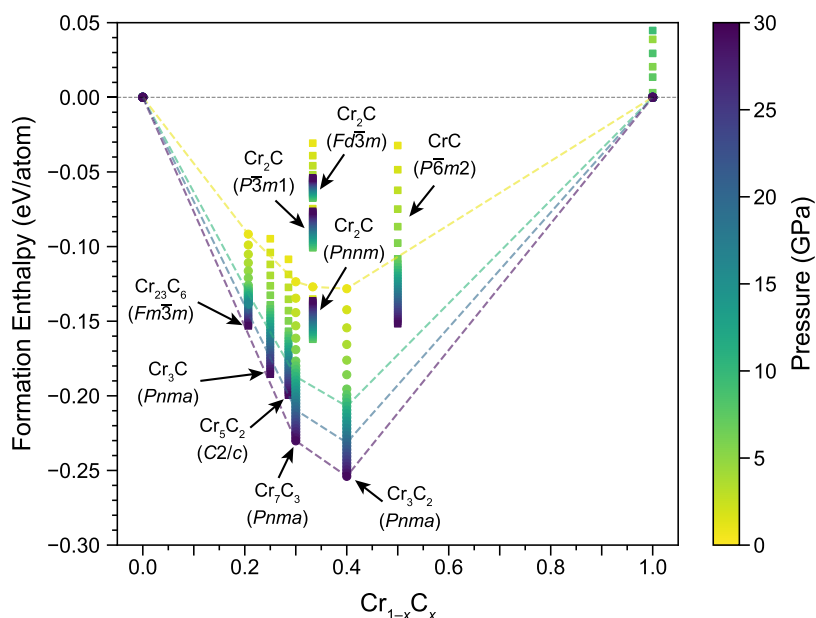
Figure 2. Calculated formation enthalpy of selected chromium carbide phases between 0 and 30 GPa, plotted in steps of 1 GPa. The allotropes of Cr and C with the lowest energy at each pressure were used as reference states. Cr was bcc for all pressures, while C was graphite for 0−6 GPa and diamond for 7−30 GPa. Phases that lie on the convex hull are plotted as circles, while metastable phases that lie above the convex hull are plotted as squares. The convex hull is plotted as a dashed line for 0, 10, 20, and 30 GPa. Data are colored according to pressure, as indicated by the color scale on the right of the figure. See the Supporting Information for details on all structures considered. The green points at $x = 1$ are the different carbon allotropes as they leave/approach the convex hull.
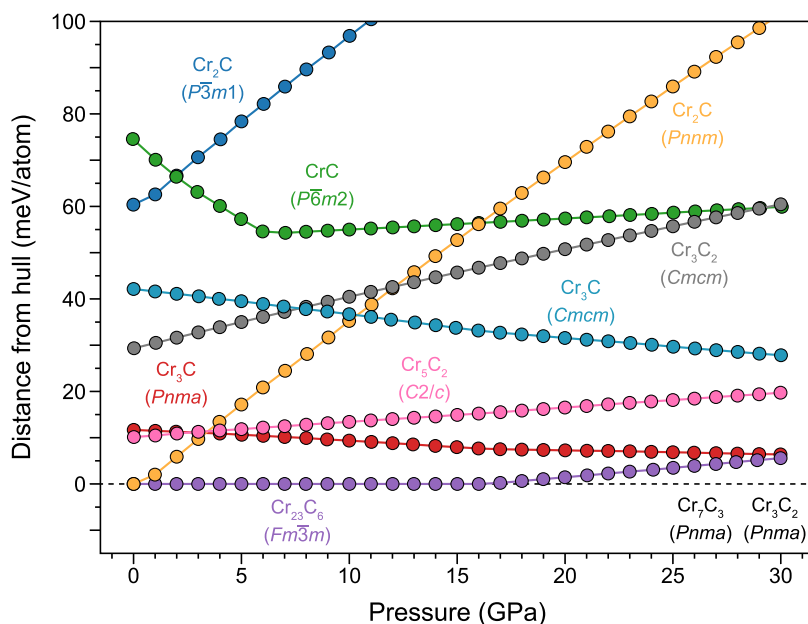

Figure 3. Plot of the calculated distance from the convex hull for selected Cr−C phases between 0 and 30 GPa. The data points for each phase are plotted in unique colors, with lines joining the points as a guide. Data points are not plotted for Cr_7C_3 (*Pnma*) and Cr_3C_2 (*Pnma*), which both remained on the convex hull over the entire pressure range plotted.

transition metal boride, carbide, and nitride systems (see the Supporting Information) and (2) a pool of randomly generated structures found using the AIRSS software package.[59,60] The random structure searches were carried out at pressures of 0, 10, 20, and 30 GPa, and although they found a large number of Cr−C phases—consistent with the known stability of chromium carbides in general—they did not find any low-energy structures that were not already included in the seeded list of phases. The low-energy structures were then recalculated

over 1 GPa steps between 0 and 30 GPa using higher precision calculations (see the Methods section). Figure 2 plots the formation enthalpies of these selected phases between 0 and 30 GPa, with the convex hull being constructed at pressures of 0, 10, 20, and 30 GPa.

At 0 GPa, the calculations are consistent with the known phases reported in the literature, with $Cr_{23}C_6$ ($Fm\bar{3}m$), Cr_7C_3 (*Pnma*), and Cr_3C_2 (*Pnma*) all appearing on the convex hull. Notably, the η-Fe$_2$C-type Cr_2C (*Pnnm*) also appears on the

hull at 0 GPa, indicating that it should be synthetically accessible. The cementite analog, Cr_3C (*Pnma*), and the chromium Hägg carbide, Cr_5C_2 (*C2/c*), both lie just above the hull, with energy differences of 12 meV atom^{-1} and 10 meV atom^{-1}, respectively.

Figure 3 plots the distance from the hull as a function of pressure for selected compounds. The three experimentally known phases remain on the hull up to 17 GPa, at which point $Cr_{23}C_6$ (*Fm$\bar{3}$m*) lifts from the hull. Cr_7C_3 (*Pnma*) and Cr_3C_2 (*Pnma*) remain on the hull over the entire range studied here. The η-Fe_2C Cr_2C (*Pnnm*) phase, which is not seen experimentally at ambient pressure, begins on the convex hull but then lifts sharply from the hull above 0 GPa. The metastable Cr_3C (*Pnma*) begins at 12 meV atom^{-1} above the hull at 0 GPa and then gradually falls closer to the hull as the pressure is increased. Cr_5C_2 (*C2/c*) starts at 10 meV atom^{-1} above the hull and increases its distance from the hull as the pressure increases. See the Supporting Information for complete details of distances from the hull.

CrC (*Fm$\bar{3}$m*) has been observed as a metastable phase in experiments,[28−30] but it is not a low-energy structure in our searches. It is at least 248 meV atom^{-1} above the hull over the pressure range calculated. Cr_2C (*Fd$\bar{3}$m*) is an ordered supercell of the NaCl-type structure that has been observed experimentally in the metal-rich side of the Zr−C and Ti−C systems.[61−64] This phase begins 96 meV atom^{-1} above the hull at 0 GPa, which is lower energy than stoichiometric CrC (*Fm$\bar{3}$m*), but it increases to 184 meV atom^{-1} above the hull at 30 GPa. This behavior is consistent with the stability of the Zr_2C (*Fd$\bar{3}$m*) phase in the substoichiometric NaCl-type Zr−C system, where Zr_2C is initially stable relative to fully stoichiometric ZrC and decreases in stability with increasing pressure.[65] Thus, our calculations are seemingly at odds with the experimental observation of this phase.

Taken together, the results of our preliminary crystal structure prediction calculations indicate that the metastable cementite Cr_3C (*Pnma*) phase could become synthetically accessible at high pressures, especially since its proximity to the convex hull is small compared to the additional energy expected from a finite temperature (i.e., these calculations are performed at zero kelvin and therefore may not accurately reflect the true potential energy surface that is relevant at higher temperatures). Based upon these results, we set out to synthesize Cr_3C (*Pnma*) in bulk form under high pressure. We did not expect to see any other phases, except for the known stable phases that exist on the hull at ambient pressure.

Laser-Heated Synthesis in the Diamond Anvil Cell

The crowded nature of the convex hull in the Cr−C system presents a technical challenge to synthesis and enforces the need for a precise control of chemical composition to avoid the formation of competing phases. This challenge is especially pronounced for high-pressure synthesis in the diamond anvil cell, where the overall composition and degree of element mixing is usually poorly constrained compared to traditional solid-state synthesis methods carried out on much larger scales (e.g., mm^3 versus μm^3).[66,67] In the present case, the targeted synthesis of the Cr_3C (*Pnma*) phase in the diamond anvil cell required us to target a precise 3:1 Cr:C precursor composition to avoid synthesizing $Cr_{23}C_6$ (*Fm$\bar{3}$m*) and Cr_7C_3 (*Pnma*), which have similar Cr:C ratios. This motivated us to develop a new approach to precursor preparation—one that we hope will

also provide a platform for a more precise and repeatable exploration of high-pressure phase space in general.

Inspired by work carried out by geophysicists,[68] we used magnetron sputtering to co-deposit chromium and carbon onto silicon, selecting deposition rates that led to a 3:1 Cr:C composition in the deposited film (see the Methods section and the Supporting Information). We deposited films with a total thickness of ∼2.5 μm. Individual flakes were lifted from the substrate and loaded into diamond anvil cells, where they were sandwiched between two laser-cut disks of (100)-oriented magnesium oxide, which acted as both a thermal insulator and a pressure calibrant. The reactivity of these sputtered flakes under high pressures was studied using the laser-heated diamond anvil cell method at HPCAT beamline 16-ID-B.[56]

We report here four separate heating experiments carried out within a single diamond anvil cell across different regions of the same sputtered sample flake. We performed each experiment at different pressures (13.5, 15.5, 20.2, and 24.3 GPa), adjusting the pressure of the cell between heating runs. In all runs, maximum temperatures of 1700−2100 K were reached, with total heating times on the order of 10−20 min. Temperature was quenched by turning off the lasers at the end of each heating run. Changes in the diffraction patterns were generally not observed below ∼1000 K, regardless of the starting pressure. At or above ∼1000 K, bcc-Cr was observed crystallizing from the amorphous signal, as evidenced by the growth and sharpening of bcc-Cr reflections. This acted somewhat as a fiducial in all of our experiments and defined the starting point of the synthesis.

The first heating run was carried out at ∼13.3 GPa. Within a few seconds of chromium annealing, we observed the steady growth of peaks that could be readily matched to the cementite Cr_3C (*Pnma*) phase (Figure S25). The temperature was measured as ∼1200−1400 K at the time that this phase crystallized. After holding for ∼2 min, we then continued to increase the laser power, and as we reached ∼1600−1800 K, we observed the growth of a second set of peaks, with a simultaneous decrease in the intensity of the Cr_3C (*Pnma*) peaks. The new peaks were not a match to any of the experimentally known phases or to any of the low-energy phases examined in our calculations. However, we could readily index the new family of peaks as belonging to a monoclinic crystal system. The lasers were then turned off after a few minutes. After thermally quenching the reaction, both the Cr_3C (*Pnma*) and monoclinic phase peaks remained, and new peaks appeared that could be readily matched to Cr_3C_2 (*Pnma*)—one of the three phases calculated to be on the convex hull at this pressure.

Our second heating run was carried out on a different region of the same sputtered flake at a pressure of ∼16.3 GPa. As with the first heating run, we initially observed the crystallization of bcc-Cr, followed by the growth of peaks from Cr_3C (*Pnma*) above ∼1200 to 1400 K, and then by peaks consistent with the monoclinic phase observed in the first heating run at higher temperatures (∼1600−1800 K). The reaction was thermally quenched after a few minutes had passed with no further changes to the diffraction patterns. After thermally quenching the reaction, we again observed the growth of the peaks from Cr_3C_2 (*Pnma*). The results of the first two heating runs were thus qualitatively the same, and although this is perhaps not surprising given how close the pressures were, the repeatability of the complex phase transformations is an encouraging

indication that composition was well constrained in our experiments. It is also worth noting here that each new region was unaffected by previous heating runs, with all sites yielding identical preheating diffraction patterns. This provides further support to the homogeneity of the sputtered sample flakes.

We next increased the pressure in the cell to ~20.0 GPa. In this run, we once again observed the annealing of bcc-Cr, followed by the appearance of Cr_3C (*Pnma*) above ~1200−1400 K and then by the monoclinic phase at ~1600−1800 K. However, we then observed the growth of peaks matching the cubic CrC ($Fm\overline{3}m$) phase immediately following the growth of the monoclinic phase (i.e., without any further increase in the temperature). This phase was completely unexpected from our crystal structure predictions, which calculated CrC ($Fm\overline{3}m$) to have a formation enthalpy of no less than 248 meV above the hull over the studied pressures. The peaks from all three of the phases that grew in were retained after thermally quenching the reaction, and Cr_3C_2 (*Pnma*) once again appeared in the postheating diffraction pattern.

Our final heating experiment was carried out at ~24.4 GPa and produced qualitatively similar results to the reaction carried out at 20.2 GPa, with Cr_3C (*Pnma*) appearing first above ~1200−1400 K (albeit with noticeably weaker intensities than at lower pressures), followed by the monoclinic phase above ~1600−1800 K, and then immediately by the CrC ($Fm\overline{3}m$). All of the phases were retained after thermal quenching. In this run, we did not observe peaks from Cr_3C_2 (*Pnma*) after cooling.

Figure 4 plots the X-ray diffraction data collected at each heating spot after the reaction was thermally quenched, and the laser table was removed from the X-ray path. These patterns are generally higher quality than those measured *in situ*, since absorption and scattering from the laser optics are removed, and the cell is able to rotate freely to achieve better orientation statistics and signal-to-noise ratio. Each of the four patterns were modeled using Rietveld methods, which allowed us to extract fitted lattice parameters for all of the identified phases.

To summarize the experimental LH-DAC results, we observed a total of four chromium carbide phases over the pressure range of 13.5 to 24.3 GPa, three of which are metastable phases that cannot be accessed under ambient pressures. Of the three thermodynamically stable phases already known from experiment, which our calculations predicted would remain on the hull over at least some of this range, only one of these, (Cr_3C_2 (*Pnma*)), was observed, and only after thermally quenching the reactions. The Cr_3C (*Pnma*) phase that was predicted to be accessible at higher pressure was observed experimentally at temperatures above ~1200−1300 K, which is in good agreement with calculations. However, the monoclinic phase and CrC ($Fm\overline{3}m$), both of which grew above ~1600−1700 K, could not have been expected from our calculations. To investigate this discrepancy, and to reconcile our experimental observations with our crystal structure predictions, we returned to theoretical methods.

Assessing the Stability of NaCl-Type CrC

While the CrC ($Fm\overline{3}m$) phase would not be expected from our initial convex hull calculations, the experimental results unambiguously show that it crystallizes under high temperatures at pressures above ~20 GPa. One explanation is that a large substoichiometry at the carbon site could have a significant influence on the enthalpy of the phase. Indeed,
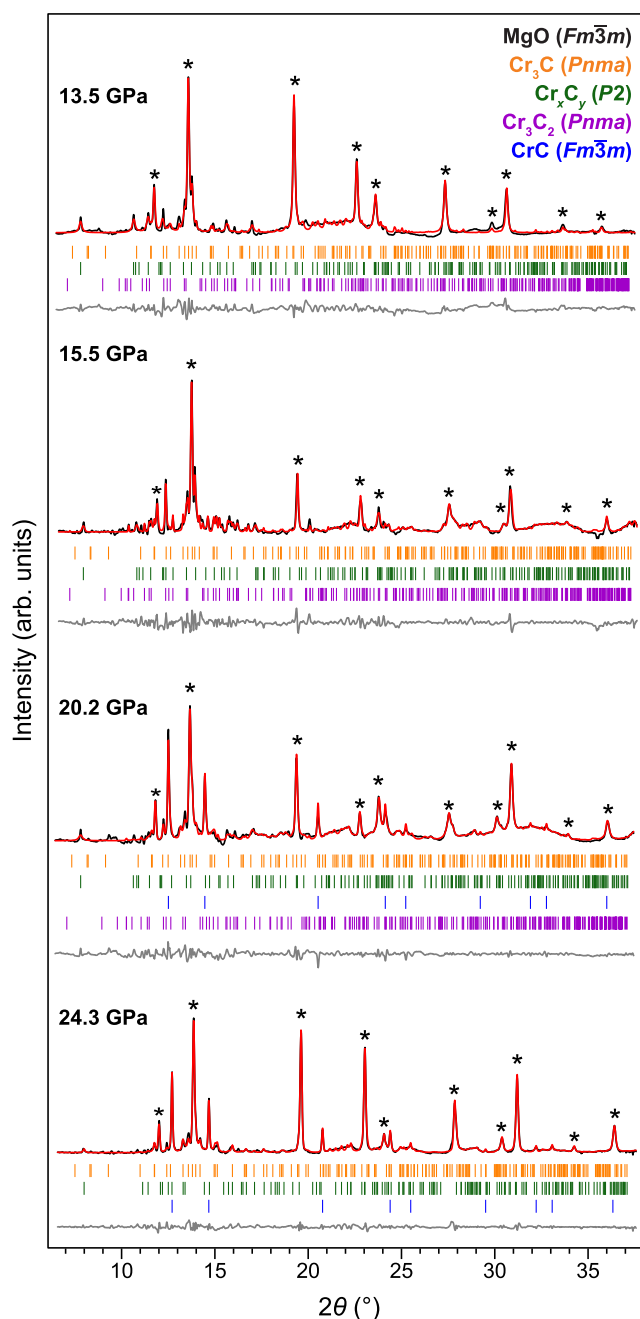

Figure 4. X-ray diffraction measured after thermal quenching at each heating site. Background subtracted experimental data are plotted in black. Rietveld methods are used to fit the multiple phases present and to extract unit cell parameters, with the modeled intensities plotted in red. Residual intensity is plotted in gray. Ticks are plotted beneath each trace to indicate the peak positions of the refined phases and are color-coded to each phase as denoted in the inset legend. Asterisks mark reflections from MgO ($Fm\overline{3}m$).

this is a common observation in many other TMCs that have been studied experimentally and computationally, with vacancy concentrations of up to 50% being typical in ZrC and TiC.[61−65,69,70]

We adopted a simple approach wherein $2 \times 2 \times 2$ supercell structures of $CrC_{(1−x)}$ ($Fm\overline{3}m$) were generated with random concentrations and configurations of vacancies at the carbon site, before being relaxed using high-throughput DFT at pressures of 0 and 20 GPa (see the Methods section for more
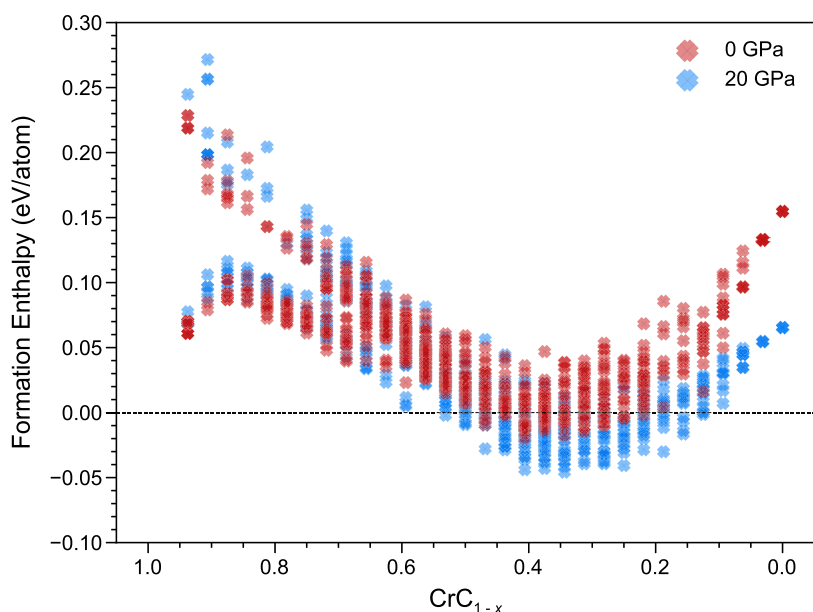
Figure 5. Formation enthalpy of random configurations of substoichiometric $CrC_{(1-x)}$ ($Fm\overline{3}m$) plotted against the composition at 0 and 20 GPa. The enthalpy reaches a minimum for both pressures at around $x = 0.35$, where the formation enthalpy of the substoichiometric carbide becomes negative. This corresponds to about $x = 0.39$ in the domain of $Cr_{1-x}C_x$ as plotted in Figure 2 and about $x = 0.65$ in the notation CrC_x.

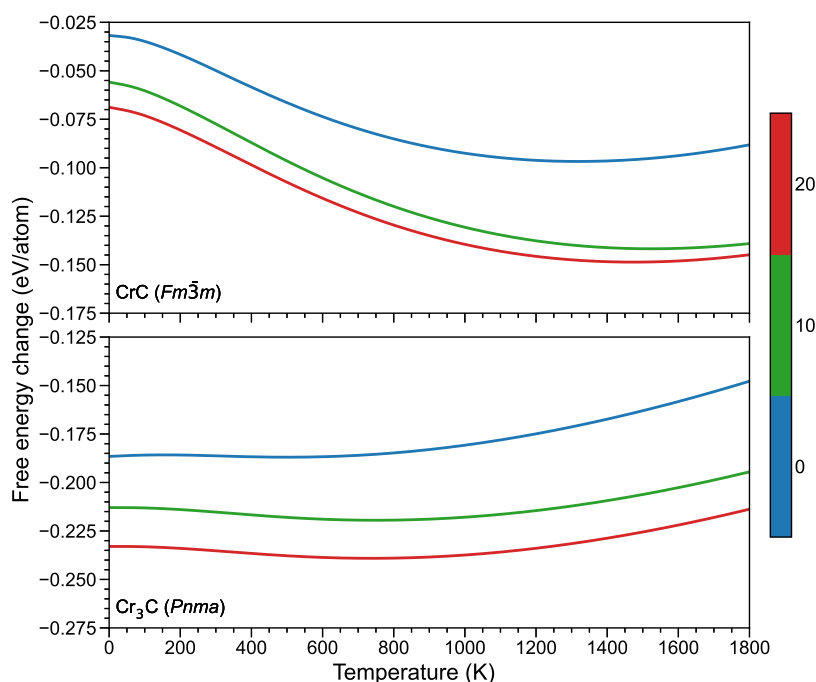**Figure 6.** Gibbs free energy of formation of the CrC ($Fm\overline{3}m$) and Cr_3C ($Pnma$) phases at 0, 10, and 20 GPa plotted against temperature. The energies are calculated from phonon density of states using Cr (bcc) and C (diamond) as reference phases. The 0 GPa data is adjusted for reference against C (graphite) using standard reference values of the enthalpy and entropy for diamond and graphite.[71] The data for CrC ($Fm\overline{3}m$) includes a term for an ideal mixing entropy with an assumed substoichiometry of $x = \frac{1}{3}$ in $CrC_{(1-x)}$ which accounts for ~ 40 meV at 1300 K.

details). The results of these calculations are plotted in Figure 5. The calculations reveal that the formation enthalpy has a significant dependence on the vacancy concentration, with a prominent dip at around $x = 0.35$ (i.e., $CrC_{0.65}$) which is a clear indication of the energetic preference for substoichiometry in this system. We note here that Rietveld refinements of the CrC phase in our XRD data using a free occupancy at the carbon site led to a value of $\sim 1/2$. However, follow-up experiments will be required before we can be confident in reporting this

parameter accurately. For both pressures, the most stable structures appear around the same vacancy concentration and, in both cases, achieve a negative formation enthalpy, with the structures at 20 GPa having a higher magnitude formation enthalpy compared to those calculated at 0 GPa. This still however does not explain why the phase is seen in experiment given that the formation enthalpy would still be around 180 meV atom^{-1} above the hull at 20 GPa even when considering the enthalpy contribution of substoichiometry.
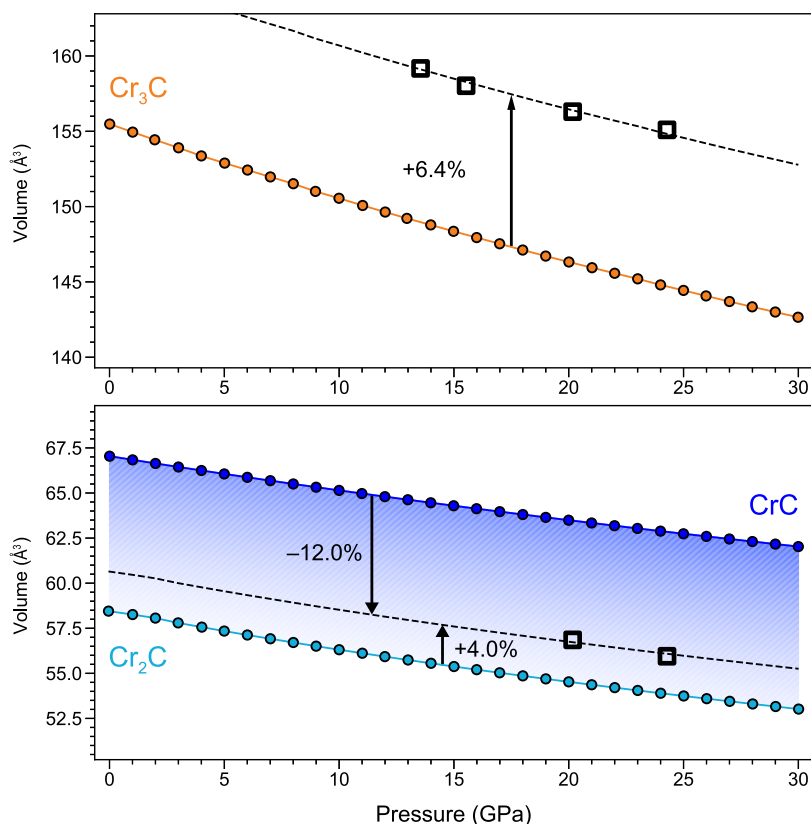
Figure 7. Plot of the experimentally determined volumes of $CrC_{(1-x)}$ ($Fm\bar{3}m$) and Cr_3C ($Pnma$) alongside volumes calculated with DFT methods. For $CrC_{(1-x)}$, we plot volumes calculated for $x = 0$ and for the ordered Cr_2C ($Fd\bar{3}m$) phase, which we use as a proxy for the disordered phase with $x = 0.5$. The mean absolute percentage error between the experimental and calculated volumes is printed, with the shifted curves plotted as dashed lines.

In order to assess the dynamical stability of the observed metastable cementite Cr_3C ($Pnma$) and NaCl-type CrC phases, we calculated the phonon dispersion relations and the phonon density of states (PDOS) at 0, 10, and 20 GPa. Both the cementite Cr_3C ($Pnma$) and NaCl-type CrC ($Fm\bar{3}m$) phases exhibit no imaginary modes, indicating that both phases are dynamically stable. The phonon calculations were conducted for the nonmagnetic phase of Cr_3C ($Pnma$) and both the nonmagnetic and the ferromagnetic phases of CrC ($Fm\bar{3}m$). The ferromagnetic phase of NaCl-type CrC ($Fm\bar{3}m$) is calculated to have lower energy and shows a noticeably larger bandwidth. All of the phonon results described above are plotted in the Supporting Information.

The phonon density of states enables an investigation into the effect that entropy, zero-point energy, and temperature have on energy, which can offer a more realistic assessment of stability as compared to calculations that use only the internal enthalpy (i.e., the zero kelvin calculations presented above). We used our PDOS to calculate the Gibbs free energy of Cr_3C ($Pnma$) and CrC ($Fm\bar{3}m$) as a function of temperature at pressures of 0, 10, and 20 GPa (see the Methods section for details), and we plot the free energy of formation for both in Figure 6. We see that the free energy of CrC decreases with increasing temperature, while the free energy of Cr_3C increases with increased temperature. Although a truly quantitative comparison would rely on a consideration of the other phases as well as a more complete treatment of substoichiometry, we can nevertheless infer from our calculations that substoichiometry both lowers the enthalpy and raises the entropy of the CrC phase, thus supporting its observation in our experiments.

Finally, Figure 7 plots the experimental lattice parameters of Cr_3C ($Pnma$) and $CrC_{(1-x)}$ ($Fm\bar{3}m$) determined from X-ray diffraction data alongside calculated pressure−volume curves from geometry optimization calculations (see the Methods section). For Cr_3C ($Pnma$), we see an underestimation of the calculated volumes with a mean absolute percentage error (MAPE) of 6.4%. For $CrC_{(1-x)}$ ($Fm\bar{3}m$), we instead see an overestimation of the calculated volume for fully stoichiometric CrC ($Fm\bar{3}m$) (i.e., $x = 0$), with a MAPE of 12%. For comparison, we also plot the calculated volumes of the ordered Cr_2C ($Fd\bar{3}m$) phase. This phase has an MAPE of 4.0% compared with the experimental volumes. The experimental volumes also agree well with the volumes of the calculated substoichiometric $CrC_{(1-x)}$ structures for around $x = 0.5$ which are plotted in Figure S11 in the Supporting Information. The low volume determined experimentally for $CrC_{(1-x)}$ could thus further support the presence of significant vacancies at the carbon site.

CONCLUSIONS

We have reported a combined first-principles and experimental investigation into the reactivity of chromium and carbon under high pressures. Crystal structure prediction methods were first employed to assess whether any novel Cr−C phases could be expected to stabilize under pressures up to 30 GPa. These calculations suggested that Cr_3C ($Pnma$) approaches the zero-kelvin convex hull under high pressures and could therefore become synthetically accessible; no other metastable phases were deemed to be promising candidates for synthesis.

We then enlisted a novel precursor preparation method using magnetron cosputtering of chromium and carbon to prepare amorphous well-mixed films with a tightly controlled 3:1 composition so that we could target the synthesis of Cr_3C (*Pnma*) while avoiding the other competing phases on the convex hull. Double-sided laser heating experiments carried out in the diamond anvil cell between pressures of 13.5–25.2 GPa on a flake of the cosputtered precursor led to the synthesis of the predicted Cr_3C (*Pnma*) phase but also to two other metastable phases: a novel monoclininc Cr–C phase and a NaCl-type CrC ($Fm\overline{3}m$).

To rationalize the unexpected appearance of the NaCl-type CrC ($Fm\overline{3}m$), which we had calculated to be very far from the convex hull, we carried out first-principles studies into the stabilizing effect of substoichiometry at the carbon site, considering both the enthalpic effects as well as the entropy effect at higher temperatures. These calculations clearly showed that the effect of vacancies is sufficient to bring this phase close to the convex hull under our synthesis conditions. The newly discovered monoclinic phase has yet to be conclusively identified, but is likely to be either a low-symmetry phase with a large number of atoms in its primitive cell (i.e., more than we can include in our random structure searching approach); a phase that becomes competitive under high temperatures; or a highly substoichiometric form of a simple phase that had been generated by our searches but which was simulated without carbon vacancies. It may also exhibit some combination of all of these factors.

In summary, we have shown that even in complicated systems such as Cr–C, where a large number of competing thermodynamic phases are already known, high pressures still offer a broad space for discovery. Our novel codeposition method for the preparation of stoichiometrically precise precursors is a promising tool for such systems, and we hope that it will enable the selective and high-yield synthesis of other phases being targeted with diamond anvil cell methods. This new synthetic handle on composition could also open the door to studying complicated ternary and quaternary systems under pressure or the use of site doping as a method for tuning the intrinsic properties and stabilities of metastable high-pressure phases.

■ ASSOCIATED CONTENT

ⓢ Supporting Information

The Supporting Information is available free of charge at https://pubs.acs.org/doi/10.1021/acsmaterialsau.3c00086.

Calculation and experimental details; Rietveld refinement details; random structure searches; convex hull plots; formation enthalpy plots; volume plots with substoichiometry; phonon dispersion and density of states plots; sputtering deposition rates; experimental setup illustrations; X-ray diffraction waterfall plots with difference traces; structure details with structure prototypes; tables of formation enthalpy distances from hull; and tables of Rietveld refinements (PDF)

■ AUTHOR INFORMATION

Corresponding Author

James P. S. Walsh − *Department of Chemistry, University of Massachusetts Amherst, Amherst, Massachusetts 01003, United States;* ⓞ orcid.org/0000-0003-3454-3428; Email: jpswalsh@umass.edu

Authors

Paul V. Marshall − *Department of Chemistry, University of Massachusetts Amherst, Amherst, Massachusetts 01003, United States;* ⓞ orcid.org/0000-0002-8332-8591

Scott D. Thiel − *Department of Chemistry, University of Massachusetts Amherst, Amherst, Massachusetts 01003, United States;* ⓞ orcid.org/0000-0002-9947-0277

Elizabeth E. Cote − *Department of Chemistry, University of Massachusetts Amherst, Amherst, Massachusetts 01003, United States*

Rostislav Hrubiak − *HPCAT, X-ray Science Division, Argonne National Laboratory, Lemont, Illinois 60439, United States*

Matthew L. Whitaker − *Department of Geosciences, Stony Brook University, Stony Brook, New York 11794-2100, United States*

Yue Meng − *HPCAT, X-ray Science Division, Argonne National Laboratory, Lemont, Illinois 60439, United States*

Complete contact information is available at:
https://pubs.acs.org/10.1021/acsmaterialsau.3c00086

Author Contributions

‖P.V.M. and S.D.T. contributed equally to this work.

Notes

The authors declare no competing financial interest.

■ REFERENCES

(1) Williams, W. S. Transition-metal carbides. *Prog. Solid State Chem.* **1971**, *6*, 57–118.

(2) Oyama, S. T. *Introduction to the Chemistry of Transition Metal Carbides and Nitrides*; Springer, 1996.

(3) Schwarz, K. Band structure and chemical bonding in transition metal carbides and nitrides. *Crit. Rev. Solid State Mater. Sci.* **1987**, *13*, 211–257.

(4) Wang, M.; Feng, Z.; Zhai, C.; Zhou, Q.; Wei, T.; Liu, J. Chromium carbide micro-whiskers: Preparation and strengthening effects in extreme conditions with experiments and molecular dynamics simulations. *J. Solid State Chem.* **2020**, *291*, No. 121598.

(5) Qing, H.; Wu, Z.; Li, H.; Guo, H.; Chen, Y. Preparation of chromium carbide coatings on graphite via powder immersion reaction assisted coating. *Ceram. Int.* **2021**, *47*, 33725–33730.

(6) Matthews, S.; James, B.; Hyland, M. The role of microstructure in the high temperature oxidation mechanism of Cr_3C_2-NiCr composite coatings. *Corros. Sci.* **2009**, *51*, 1172–1180.

(7) Murthy, J.; Bysakh, S.; Gopinath, K.; Venkataraman, B. Microstructure dependent erosion in (Cr_3C_2)−20 (NiCr) coating deposited by a detonation gun. *Surf. Coat. Technol.* **2007**, *202*, 1–12.

(8) Huang, Z.; Ma, S.; Xing, J.; Sun, S. Bulk Cr_7C_3 compound fabricated by mechanical ball milling and plasma activated sintering. *Int. J. Refract. Met. Hard Mater.* **2014**, *45*, 204−211.

(9) Liu, X.-B.; Wang, H.-M. Microstructure and tribological properties of laser clad $\gamma/Cr_7C_3/TiC$ composite coatings on γ-TiAl intermetallic alloy. *Wear* **2007**, *262*, 514−521.

(10) Zikin, A.; Hussainova, I.; Katsich, C.; Badisch, E.; Tomastik, C. Advanced chromium carbide-based hardfacings. *Surf. Coat. Technol.* **2012**, *206*, 4270−4278.

(11) Hussainova, I.; Jasiuk, I.; Sardela, M.; Antonov, M. Micro-mechanical properties and erosive wear performance of chromium carbide based cermets. *Wear* **2009**, *267*, 152−159.

(12) Nygren, K.; Samuelsson, M.; Flink, A.; Ljungcrantz, H.; Rudolphi, K.; Jansson, U. Growth and characterization of chromium carbide films deposited by high rate reactive magnetron sputtering for electrical contact applications. *Surf. Coat. Technol.* **2014**, *260*, 326−334.

(13) Li, T.; Ma, C.; Li, Y.; Tu, F.; Jiao, C.; Li, Z.; Yao, S. In situ preparation of chromium carbide−modified carbon nanofibers as functional electrocatalyst for polysulfide reduction in lithium/sulfur batteries. *Ionics* **2022**, *28*, 1701−1711.

(14) Moissan, H. A Fast Preparation of Chromium and Manganese at High Temperature. *C. R. Hebd. Seances Acad. Sci.* **1893**, *116*, 349−351.

(15) Guilemany, J.; Miguel, J.; Vizcaíno, S.; Lorenzana, C.; Delgado, J.; Sánchez, J. Role of heat treatments in the improvement of the sliding wear properties of Cr_3C_2−NiCr coatings. *Surf. Coat. Technol.* **2002**, *157*, 207−213.

(16) Moissan, H. New Investigations Concerning Chromium. *C. R. Hebd. Seances Acad. Sci.* **1894**, *119*, 185−191.

(17) Bowman, A. L.; Arnold, G.; Storms, E.; Nereson, N. The crystal structure of $Cr_{23}C_6$. *Acta Crystallogr., Sect. B: Struct. Crystallogr. Cryst. Chem.* **1972**, *28*, 3102−3103.

(18) Ruff, O.; Foehr, T. Chromium and Carbon. *Z. Anorg. Allg. Chem.* **1918**, *104*, 27−46.

(19) Rouault, A.; Herpin, P.; Fruchart, R. Études christallographique des carbures Cr_7C_3 et Mn_7C_3. *Ann. Chim.* **1970**, *5*, 461−470.

(20) Inoue, A.; Masumoto, T. Formation of nonequilibrium Cr_3C carbide in Cr−C binary alloys quenched rapidly from the melt. *Scr. Metall. Mater.* **1979**, *13*, 711−715.

(21) Fernández Guillermet, A. Predictive approach to thermodynamic properties of the metastable Cr_3C Carbide. *Int. J. Thermophys.* **1991**, *12*, 919−936.

(22) Ganguly, A.; Murthy, V.; Kannoorpatti, K. Structural and electronic properties of chromium carbides and Fe-substituted chromium carbides. *Mater. Res. Express* **2020**, *7*, No. 056508.

(23) Xu, Z.; Lv, X.; Chen, J.; Jiang, L.; Lai, Y.; Li, J. DFT investigation of capacious, ultrafast and highly conductive hexagonal Cr_2C and V_2C monolayers as anode materials for high-performance lithium-ion batteries. *Phys. Chem. Chem. Phys.* **2017**, *19*, 7807−7819.

(24) Bouzy, E.; Le Caër, G.; Bauer-Grosse, E. New metastable carbides produced by crystallization of amorphous Cr−C alloys. *Mater. Sci. Eng., A* **1991**, *133*, 640−643.

(25) Bouzy, E. Structures et défauts des carbures produits par la cristallisation d'alliages amorphes chrome-carbone, Theses. Institut National Polytechnique de Lorraine, 1990.

(26) Wang, D.-Y.; Weng, K.-W.; Chang, C.-L.; Ho, W.-Y. Synthesis of Cr_3C_2 coatings for tribological applications. *Surf. Coat. Technol.* **1999**, *120−121*, 622−628.

(27) Jellad, A.; Labdi, S.; Malibert, C.; Renou, G. Nanomechanical and nanowear properties of Cr_3C_2 thin films deposited by rf sputtering. *Wear* **2008**, *264*, 893−898.

(28) Wang, J.; Chen, X.; Yang, N.; Fang, Z. Formation of NaCl-type Cr carbide by carbon ion implantation. *Appl. Phys. A: Solids Surf.* **1993**, *56*, 307−309.

(29) Liu, B. X.; Cheng, X. Y. A metastable Cr carbide of NaCl structure formed by carbon-ion implantation into chromium films. *J. Phys.: Condens. Matter* **1992**, *4*, L265−L268.

(30) Bewilogua, K.; Heinitz, H.-J.; Rau, B.; Schulze, S. A chromium carbide phase with B1 structure in thin films prepared by ion plating. *Thin Solid Films* **1988**, *167*, 233−244.

(31) Marshall, P. V.; Alptekin, Z.; Thiel, S. D.; Smith, D.; Meng, Y.; Walsh, J. P. S. High-Pressure Synthesis of Bulk Cobalt Cementite, Co_3C. *Chem. Mater.* **2021**, *33*, 9601−9607.

(32) Arpita Aparajita, A.; Sanjay Kumar, N.; Chandra, S.; Chandra Shekar, N.; Kalavathi, S. Synthesis of novel chromium carbide using laser heated diamond anvil cell. *J. Solid State Chem.* **2021**, *295*, 121899.

(33) Friedrich, A.; Winkler, B.; Juarez-Arellano, E. A.; Bayarjargal, L. Synthesis of binary transition metal nitrides, carbides and borides from the elements in the laser-heated diamond anvil cell and their structure-property relations. *Materials* **2011**, *4*, 1648−1692.

(34) Fedotenko, T.; Khandarkhaeva, S.; Dubrovinsky, L.; Glazyrin, K.; Sedmak, P.; Dubrovinskaia, N. Synthesis and Compressibility of Novel Nickel Carbide at Pressures of Earth's Outer Core. *Minerals* **2021**, *11*, 516.

(35) Ono, S.; Kikegawa, T.; Ohishi, Y. A high-pressure and high-temperature synthesis of platinum carbide. *Solid State Commun.* **2005**, *133*, 55−59.

(36) Kurakevych, O. O.; Strobel, T. A.; Kim, D. Y.; Cody, G. D. Synthesis of Mg_2C: A Magnesium Methanide. *Angew. Chem.* **2013**, *125*, 9098−9101.

(37) Tsuzuki, A.; Sago, S.; Hirano, S. I.; Naka, S. High temperature and pressure preparation and properties of iron carbides Fe_7C_3 and Fe_3C. *J. Mater. Sci.* **1984**, *19*, 2513−2518.

(38) Kumar, N. R. S.; Shekar, N. V. C.; Chandra, S.; Basu, J.; Divakar, R.; Sahu, P. C. Synthesis of novel Ru_2C under high pressure−high temperature conditions. *J. Phys.: Condens. Matter* **2012**, *24*, No. 362202.

(39) Kumar, N. R. S.; Chandra, S.; Amirthapandian, S.; Shekar, N. V. C.; Sahu, P. C. Investigations of the high pressure synthesized osmium carbide by experimental and computational techniques. *Mater. Res. Express* **2015**, *2*, No. 016503.

(40) Zhao, Z.; Cui, L.; Wang, L.-M.; Xu, B.; Liu, Z.; Yu, D.; He, J.; Zhou, X.-F.; Wang, H.-T.; Tian, Y. Bulk Re_2C: Crystal Structure, Hardness, and Ultra-incompressibility. *Cryst. Growth Des.* **2010**, *10*, 5024−5026.

(41) Clark, S. J.; Segall, M. D.; Pickard, C. J.; Hasnip, P. J.; Probert, M. I. J.; Refson, K.; Payne, M. C. First principles methods using CASTEP. *Z. Kristallogr. - Cryst. Mater.* **2005**, *220*, 567−570.

(42) Monkhorst, H. J.; Pack, J. D. Special points for Brillouin-zone integrations. *Phys. Rev. B* **1976**, *13*, 5188.

(43) Kunc, K.; Martin, R. M. *Ab initio* force constants of GaAs: A new approach to calculation of phonons and dielectric properties. *Phys. Rev. Lett.* **1982**, *48*, 406−409.

(44) Frank, W.; Elsässer, C.; Fähnle, M. Ab initio Force-Constant Method for Phonon Dispersions in Alkali Metals. *Phys. Rev. Lett.* **1995**, *74*, 1791−1794.

(45) Parlinski, K.; Li, Z. Q.; Kawazoe, Y. First-Principles Determination of the Soft Mode in Cubic ZrO_2. *Phys. Rev. Lett.* **1997**, *78*, 4063−4066.

(46) Born, M.; Huang, K.; Lax, M. Dynamical Theory of Crystal Lattices. *Am. J. Phys.* **1955**, *23*, 474.

(47) Gonze, X.; Lee, C. Dynamical matrices, Born effective charges, dielectric permittivity tensors, and interatomic force constants from density-functional perturbation theory. *Phys. Rev. B* **1997**, *55*, 10355−10368.

(48) Perdew, J. P.; Burke, K.; Ernzerhof, M. Generalized Gradient Approximation Made Simple. *Phys. Rev. Lett.* **1996**, *77*, 3865−3868.

(49) Rutter, M. C2x: A tool for visualisation and input preparation for Castep and other electronic structure codes. *Comput. Phys. Commun.* **2018**, *225*, 174−179.

(50) Larsen, A. H.; Mortensen, J. J.; Blomqvist, J.; Castelli, I. E.; Christensen, R.; Dułak, M.; Friis, J.; Groves, M. N.; Hammer, B.; Hargus, C.; Hermes, E. D.; Jennings, P. C.; Jensen, P. B.; Kermode, J.; Kitchin, J. R.; Kolsbjerg, E. L.; Kubal, J.; Kaasbjerg, K.; Lysgaard, S.; Maronsson, J. B.; Maxson, T.; Olsen, T.; Pastewka, L.; Peterson, A.;

Rostgaard, C.; Schiøtz, J.; Schütt, O.; Strange, M.; Thygesen, K. S.; Vegge, T.; Vilhelmsen, L.; Walter, M.; Zeng, Z.; Jacobsen, K. W. The atomic simulation environment − a Python library for working with atoms. *J. Phys.: Condens. Matter* **2017**, *29*, No. 273002.

(51) Ong, S. P.; Richards, W. D.; Jain, A.; Hautier, G.; Kocher, M.; Cholia, S.; Gunter, D.; Chevrier, V. L.; Persson, K. A.; Ceder, G. Python Materials Genomics (pymatgen): A robust, open-source python library for materials analysis. *Comput. Mater. Sci.* **2013**, *68*, 314−319.

(52) Mehl, M. J.; Hicks, D.; Toher, C.; Levy, O.; Hanson, R. M.; Hart, G.; Curtarolo, S. The AFLOW Library of Crystallographic Prototypes: Part 1. *Comput. Mater. Sci.* **2017**, *136*, S1−S828.

(53) Hicks, D.; Mehl, M. J.; Gossett, E.; Toher, C.; Levy, O.; Hanson, R. M.; Hart, G.; Curtarolo, S. The AFLOW Library of Crystallographic Prototypes: Part 2. *Comput. Mater. Sci.* **2019**, *161*, S1−S1011.

(54) Hicks, D.; Mehl, M. J.; Esters, M.; Oses, C.; Levy, O.; Hart, G. L.; Toher, C.; Curtarolo, S. The AFLOW Library of Crystallographic Prototypes: Part 3. *Comput. Mater. Sci.* **2021**, *199*, No. 110450.

(55) Esters, M.; Oses, C.; Divilov, S.; Eckert, H.; Friedrich, R.; Hicks, D.; Mehl, M. J.; Rose, F.; Smolyanyuk, A.; Calzolari, A.; Campilongo, X.; Toher, C.; Curtarolo, S. aflow.org: A web ecosystem of databases, software and tools. *Comput. Mater. Sci.* **2023**, *216*, No. 111808.

(56) Meng, Y.; Hrubiak, R.; Rod, E.; Boehler, R.; Shen, G. New developments in laser-heated diamond anvil cell with in situ synchrotron x-ray diffraction at High Pressure Collaborative Access Team. *Rev. Sci. Instrum.* **2015**, *86*, No. 072201.

(57) Kavner, A.; Duffy, T. S. Pressure−volume−temperature paths in the laser-heated diamond anvil cell. *J. Appl. Phys.* **2001**, *89*, 1907−1914.

(58) Prescher, C.; Prakapenka, V. B. DIOPTAS: a program for reduction of two-dimensional X-ray diffraction data and data exploration. *High Pressure Res.* **2015**, *35*, 223−230.

(59) Pickard, C. J.; Needs, R. J. High-Pressure Phases of Silane. *Phys. Rev. Lett.* **2006**, *97*, No. 045504.

(60) Pickard, C. J.; Needs, R. J. Ab initio random structure searching. *J. Phys.: Condens. Matter* **2011**, *23*, No. 053201.

(61) Goretzki, H. Neutron Diffraction Studies on Titanium-Carbon and Zirconium-Carbon Alloys. *Phys. Status Solidi B* **1967**, *20*, K141−K143.

(62) Lipatnikov, V.; Rempel, A.; Gusev, A. Atomic ordering and hardness of nonstoichiometric titanium carbide. *Int. J. Refract. Met. Hard Mater.* **1997**, *15*, 61−64.

(63) Tashmetov, M.; Em, V.; Lee, C.; Shim, H.; Choi, Y.; Lee, J. Neutron diffraction study of the ordered structures of non-stoichiometric titanium carbide. *Phys. B* **2002**, *311*, 318−325.

(64) Davey, T.; Chen, Y. Vacancy ordering in substoichiometric zirconium carbide: A review. *Int. J. Ceram. Eng. Sci.* **2022**, *4*, 134−157.

(65) Thiel, S. D.; Walsh, J. P. S. First-Principles Investigation of Phase Stability in Substoichiometric Zirconium Carbide under High Pressure. *Adv. Theory Simul.* **2022**, *5*, No. 2200439.

(66) Pan, Y.; Li, N.; Yan, Y.; Shi, S.; Yan, Z.; Shi, L.; Liu, Q.; Liu, Z. Novel solid-state calcium carbide synthesis from calcium oxide and walnut shell char by in-situ induction heating. *Chem. Eng. J.* **2023**, *461*, No. 142043.

(67) Li, J.; Zhang, J.; Zhai, H.; Tang, X.; Tan, G. Rapid synthesis of garnet-type $Li_7La_3Zr_2O_{12}$ solid electrolyte with superior electro-chemical performance. *J. Eur. Ceram. Soc.* **2022**, *42*, 1568−1575.

(68) Pigott, J. S.; Ditmer, D. A.; Fischer, R. A.; Reaman, D. M.; Hrubiak, R.; Meng, Y.; Davis, R. J.; Panero, W. R. High-pressure, high-temperature equations of state using nanofabricated controlled-geometry $Ni/SiO_2/Ni$ double hot-plate samples. *Geophys. Res. Lett.* **2015**, *42*, 10,239−10,247.

(69) Tan, K. E.; Bratkovsky, A. M.; Harris, R. M.; Horsfield, A. P.; Nguyen-Manh, D.; Pettifor, D. G.; Sutton, A. P. Carbon vacancies in titanium carbide. *Modell. Simul. Mater. Sci. Eng.* **1997**, *5*, 187−198.

(70) Zueva, L. V.; Gusev, A. I. Effect of nonstoichiometry and ordering on the period of the basis structure of cubic titanium carbide. *Phys. Solid State* **1999**, *41*, 1032−1038.

(71) *CRC Handbook of Chemistry and Physics*, 104th ed.; Rumble, J., Ed.; CRC Press/Taylor & Francis, 2023.